



Connectivity Approach for Detecting Unreliable DInSAR Ice Velocity Measurements

Andersen, Jonas Kvist; Boncori, John Peter Merryman; Kusk, Anders

Published in:
IEEE Transactions on Geoscience and Remote Sensing

Link to article, DOI:
[10.1109/TGRS.2022.3169722](https://doi.org/10.1109/TGRS.2022.3169722)

Publication date:
2022

Document Version
Peer reviewed version

[Link back to DTU Orbit](#)

Citation (APA):
Andersen, J. K., Boncori, J. P. M., & Kusk, A. (2022). Connectivity Approach for Detecting Unreliable DInSAR Ice Velocity Measurements. *IEEE Transactions on Geoscience and Remote Sensing*, 60, Article 4304512. <https://doi.org/10.1109/TGRS.2022.3169722>

General rights

Copyright and moral rights for the publications made accessible in the public portal are retained by the authors and/or other copyright owners and it is a condition of accessing publications that users recognise and abide by the legal requirements associated with these rights.

- Users may download and print one copy of any publication from the public portal for the purpose of private study or research.
- You may not further distribute the material or use it for any profit-making activity or commercial gain
- You may freely distribute the URL identifying the publication in the public portal

If you believe that this document breaches copyright please contact us providing details, and we will remove access to the work immediately and investigate your claim.

Connectivity Approach for Detecting Unreliable DInSAR Ice Velocity Measurements

Jonas Kvist Andersen, John Peter Merryman Boncori, and Anders Kusk

Abstract—Differential Synthetic Aperture Radar Interferometry (DInSAR) allows for retrieval of ice velocity measurements of high resolution and accuracy. One of the main error sources in DInSAR is the phase unwrapping procedure. Unwrapping errors may be caused by several processes, including shear stresses associated with large motion gradients, which lead to loss of interferometric coherence. In many cases, unwrapping errors reach magnitudes corresponding to velocities of tens or even hundreds of meters per year. Traditional DInSAR implementations include pixel masking based on coherence thresholding, however such a masking is not always sufficient. Consequently, the state-of-the-art for ice velocity retrievals involves either manual inspection of individual measurements or simply discarding measurements in regions where ice flow exceeds a pre-defined threshold. Here, we instead apply a masking based on thresholding of a pixel connectivity estimate with respect to a reference point, which aims to detect unwrapping errors based only on the estimated coherence pattern. The method is tested on both simulated and real Sentinel-1 data from the Greenland Ice Sheet and effectively detects the majority of unwrapping errors (recall of 0.84 for the best performing threshold), although with a relatively low precision (0.52 for the best performing threshold). Importantly, higher magnitude unwrapping errors are associated with lower connectivity values, meaning that undetected errors have a significantly lower magnitude (median of 1.7 m/y, corresponding to a single phase cycle, compared to 40.5 m/y with no masking).

Index Terms—Ice velocity, interferometry, phase unwrapping, synthetic aperture radar (SAR), Sentinel-1.

I. INTRODUCTION

FOR several decades, Synthetic Aperture Radar (SAR) satellite data has been applied in the measurement of ice velocity over glaciers and ice sheets. The technique of Differential SAR Interferometry (DInSAR) generally provides measurements of higher accuracy and resolution, compared to amplitude tracking techniques, although it cannot be applied where velocity gradients are high enough to yield phase ambiguities. In such regions, tracking-based techniques must be used. Hence, the optimal scheme for ice sheet-wide velocity retrieval utilizes DInSAR where possible, supplemented by tracking-based techniques (e.g. over fast-flowing glacier outlets). Such a scheme has previously been carried out using several SAR systems (e.g. Radarsat, Radarsat-2, and ALOS-PALSAR [1], [2]). Since their launch in 2014 and 2016, respectively, the EU Copernicus Sentinel-1 satellites have been extensively used to provide routine velocity measurements over polar regions, due to the extensive coverage and low

revisit time provided by the TOPS acquisition mode [3]. Sentinel-1 routine ice velocity retrievals, however, have so far been based solely on amplitude tracking, as the TOPS mode inherently leads to a coupling between differential phase and azimuth motion, which, if not accounted for, may result in intra-burst phase gradients and inter-burst phase discontinuities [1]–[4]. A resolution to this issue was presented in [5], [6], where Sentinel-1 DInSAR and amplitude tracking measurements were combined to retrieve the ice velocity for a major Greenland drainage basin.

A remaining challenge concerning DInSAR ice velocity measurements, regardless of the SAR acquisition mode, is related to the phase unwrapping processing step. Most phase unwrapping algorithms seek to determine the correct number of 2π phase cycles to add/subtract to each pixel, so that the phase difference between any pair of image pixels is, in absence of other contributions, proportional to the underlying motion gradient in the radar line-of-sight (LoS) direction. An unwrapping error then occurs when the algorithm assigns a wrong integer multiple of phase cycles. An error of N phase cycles translates to a LoS velocity error through

$$v_{LoS,\sigma} = 2\pi N \frac{\lambda}{4\pi\Delta T} = \frac{N\lambda}{2\Delta T} \quad (1)$$

where λ is the radar wavelength and ΔT is the temporal baseline of the interferogram. For a Sentinel-1 interferogram with a 6-day baseline, an unwrapping error of a single phase cycle translates to a velocity error of about 1.7 m/y, which is already well above the achievable accuracy of DInSAR measurements [5]. Generally, however, unwrapping errors may reach magnitudes of tens of phase cycles, becoming the most significant error source in the resulting velocity measurements. Phase unwrapping errors arise due to phase differences between neighboring pixels being greater than π radians, which typically occur in and around areas exhibiting interferometric decorrelation (loss of coherence) [7]. Decorrelation may result from temporal changes between acquisitions (e.g., surface melt or precipitation), topographic effects (e.g., layover or shadow), spatial decorrelation, errors in the geometrical coregistration, and from large spatial gradients in the velocity field, as are found over many outlet glaciers [7]–[10]. The latter can lead to phase ambiguities and complete loss of coherence in areas of excessive shear stress [11]. Consequently, most phase unwrapping techniques apply a masking of the wrapped phase pixels based on some combination of coherence, phase residue density, intensity, topography, and other parameters [7], [12]. In general, however, unwrapping errors are not restricted to pixels with low coherence, high residue density, or radar

This research was funded by DTU Space, Technical University of Denmark. The authors are with DTU Space, Technical University of Denmark, 2800 Kongens Lyngby, Denmark (e-mail: jkvand@space.dtu.dk)

shadow regions, but may propagate into neighboring regions. Hence, a pixel-wise masking based on such parameters will not always successfully prevent or discard all unwrapping errors.

Another common practice for preventing unreliable DInSAR measurements, due to the risk of unwrapping errors, in ice velocity retrievals is either to avoid carrying out DInSAR in areas where velocities above a certain threshold are expected [1] or to perform a visual inspection of each individual unwrapped interferogram to detect signs of unwrapping errors [2]. It is not, however, always possible to distinguish unwrapping errors from natural velocity variations. Additionally, for ice sheet-wide monitoring applications, visual inspections would be excessively time consuming. Finally, unwrapping errors are not always limited to regions of fast flow, as will be demonstrated in Section III.

The main objective of this work is to determine a procedure for discarding unreliable DInSAR measurements within a routine processing scheme, e.g. an ice sheet-wide velocity retrieval. Therefore, the procedure should be as automated as possible, requiring little input and manual inspection from the user. In this paper, we present a masking approach based on the pixel connectivity measure, first proposed in [13]. In [13], a pixel-wise connectivity measure is presented, which measures how well a given pixel can be connected to a selected reference point through high coherence pixels. Unwrapping errors are often associated with low connectivity regions, as will also be demonstrated. The masking method is described in Section II and Section III presents a validation on simulated data. Section IV presents an application of the method on real Sentinel-1 data. Section V provides a discussion of the results and the limitations of the masking approach. Finally, Section VI presents final conclusions on the findings.

II. METHODOLOGY

A. Interferometric Processing Chain

A typical DInSAR processing chain is shown in the grey blocks in Fig. 1. The specific approach used in this paper for interferometric processing is that implemented in DTU's IPP processor [14], which actually includes several processing steps prior to phase unwrapping to reduce the occurrence and extent of phase unwrapping errors [15]. For Sentinel-1 data, a refined coregistration is applied, which is described in [5] along with the full processing algorithm. Phase unwrapping is performed via a Minimum Cost Flow (MCF) algorithm. Prior to unwrapping, weights are computed based on coherence and edge strength computed from the interferogram magnitude [16]. A mask is generated by discarding pixels with coherence below an adaptive threshold, depending on the selected number of range and azimuth looks, as well as pixels where layover or shadow effects are predicted, based on the input Digital Elevation Model (DEM). Morphological erosion with a 5-pixel cross as the structure element [15], [17], is applied to the pixels above the threshold, thereby masking out areas bordering previously discarded pixels. A segmentation based on 4-point connectivity is then used to divide valid pixels into connected segments. Phase unwrapping is then carried out, with masked pixels being assigned a minimum weight,

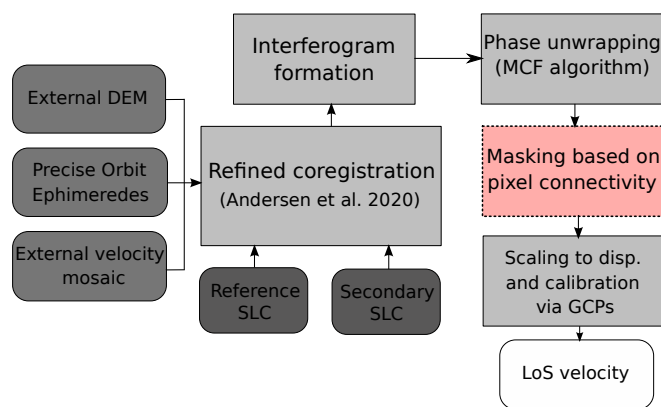


Fig. 1. Block diagram outlining the Sentinel-1 interferometric processing chain as presented in [5], with an added masking step based on pixel connectivity, described in Section II-B.

after which a baseline calibration is performed for the largest segment, followed by an absolute phase calibration of individual segments [15]. Unwrapped measurements are converted to displacement and calibrated through Ground Control Points (GCPs) selected in slow-moving areas of the ice sheet [5], [15]. Although the coherence-based masking segmentation approach is effective at preventing some unwrapping errors, it is not always enough to prevent errors in particularly challenging regions. An example of this is shown in Fig. 2a-c, where an unwrapping error is observed in a region of high coherence that is not isolated by the coherence-based segmentation approach. We propose the introduction of an additional processing step, following the phase unwrapping, which serves to improve the detection of unreliably unwrapped measurements, based on a pixel connectivity estimate, and mask them out.

B. Masking Based on Pixel Connectivity

Unwrapping errors tend to occur in segments that are separated by areas of low coherence, which in the case of glaciers and ice sheets may be caused by excessive shear stress, surface melting, or precipitation. The segmentation process described in Section II-A allows for the detection of segments that are completely disconnected from the remainder of the scene by coherence pixels below a given threshold, however regions which are only loosely connected may remain, such as the one in the top-right of Fig. 2, and these are also prone to phase unwrapping errors. To detect such regions, we apply a masking procedure based on a measure of pixel connectivity, which was previously introduced in [13] in the context of topographic estimation. The connectivity defines how well each pixel is connected to a selected reference point based on a confidence map, i.e. a pixel-wise quality measure. An obvious choice for the confidence map is the interferometric coherence, as this is a general measure of phase quality, and, as previously mentioned, unwrapping errors are prevalent in areas that are disconnected by low coherence values. The connectivity at a specific pixel is then simply defined as the lowest coherence value encountered on the best available path to the reference point (i.e. the path with the highest minimum

188 coherence value). Thus, the connectivity between a certain
 189 pixel and the reference point is high if they can be connected
 190 by a path of exclusively high coherence values. Conversely,
 191 a low connectivity is obtained if the two pixels can only be
 192 connected by paths which propagate through low coherence
 193 values.

194 Fig. 2d shows the connectivity map derived from the co-
 195 herence with the reference point shown by the red dot. The
 196 coherence image contains a zone of low values, corresponding
 197 to a shear margin, and connectivity is observed to be low for
 198 pixels on the opposite side of the shear margin, with respect to
 199 the reference point. This region of low connectivity is seen to
 200 be associated with a large magnitude unwrapping error, which
 201 is not isolated by the coherence-based segmentation mask.
 202 Hence, such an error would not be corrected or discarded by
 203 the conventional unwrapping approach, but would be discarded
 204 by applying a masking of pixels with a connectivity below a
 205 certain threshold. In practice, the connectivity map is com-
 206 puted through Dijkstra’s single source shortest path algorithm
 207 [13], [18], implemented using a heap queue, which allows for
 208 relatively fast computation of the connectivity map (a fraction
 209 of the processing time needed for unwrapping).

210 Concerning the exploitation of the connectivity concept
 211 within a DInSAR processing chain, it is suggested (although
 212 not demonstrated) in [13] to correct large-scale unwrapping
 213 errors by computing connectivity maps based on several
 214 manually selected reference points followed by a calibration
 215 with GCPs in each region. The algorithm does not, however,
 216 provide a way of quantifying a connectivity threshold be-
 217 low which measurements are marked as unwrapping errors.
 218 Furthermore, for ice velocity applications, such a correction
 219 approach would require the availability of a dense network of
 220 GCPs where motion is known to within a single phase cycle
 221 (1.7 m/y for a Sentinel-1 6-day image pair), which is not
 222 realistic. The approach we propose consists of computation
 223 of the connectivity estimate based on a single reference
 224 point, followed by a masking of pixels below a connectivity
 225 threshold, ϵ_c , which are then deemed unreliable. For the pixel-
 226 wise confidence measure used to estimate the connectivity,
 227 we experimented with various weighting functions applied
 228 to the coherence (e.g. thresholding or sigmoidal weighting
 229 functions), however the best results were found using the
 230 unweighted coherence. As the computation of connectivity
 231 requires only the coherence image, one could choose to apply
 232 the connectivity mask to the wrapped phase prior to phase
 233 unwrapping. In practice, however, we found that the MCF
 234 unwrapping algorithm performs better when applying the mask
 235 after unwrapping, as indicated by the red box in Fig. 1. In
 236 some instances, low coherence patches of a relatively small
 237 spatial extent, which are typically not observed to cause
 238 unwrapping errors, lead to low connectivity values in nearby
 239 pixels. To avoid masking out these generally unproblematic
 240 measurements, we apply a morphological closing to the binary
 241 connectivity mask before applying it. A simulated data set is
 242 used to estimate the best performing connectivity threshold,
 243 as presented in Section III.

III. VALIDATION ON SIMULATED DATA

244

245 In some cases, unwrapping errors may be easily recog-
 246 nizable in the LoS velocity estimate, e.g. in cases where
 247 the velocity field shows magnitudes or gradients that are
 248 unrealistic (based on a priori knowledge, e.g. an average
 249 velocity mosaic). In general, however, recognition may be
 250 complicated by seasonal variation in the velocity field. Further-
 251 more, other potential error sources such as calibration errors
 252 are superimposed on any unwrapping errors. Therefore, to
 253 quantitatively examine the occurrence of unwrapping errors,
 254 and thus to allow for a validation of the connectivity masking
 255 method, we generate simulated interferometric pairs of Single
 256 Look Complex (SLC) SAR images based on realistic coher-
 257 ence estimates. The simulation procedure is described in the
 258 Appendix and outlined in Fig. 3. Each simulated interferogram
 259 contains phase contributions from speckle (estimated through
 260 the observed coherence of a real Sentinel-1 image pair),
 261 topography (computed through a DEM), and a known velocity
 262 field (a LoS-projection of a multi-year average velocity mosaic
 263 derived with SAR offset tracking). While seasonal changes
 264 in surface properties are represented by the real coherence
 265 estimates used in simulating the interferograms, the motion
 266 input phase contribution does not include seasonal variations,
 267 as these are not expected to affect the general distribution
 268 of unwrapping errors. Furthermore, the simulations do not
 269 contain phase contributions from tropospheric and ionospheric
 270 effects. Although these are of course important error sources
 271 in DInSAR, they are not in general expected to cause phase
 272 unwrapping errors, due to the high degree of spatial correla-
 273 tion. Finally, the SLC simulation does not take into account the
 274 observed backscatter intensity, as variations associated with an
 275 increased likelihood of phase jumps (e.g. in layover or shadow
 276 areas) would also be characterized by the coherence.

277 The simulated SLCs are input to the processing chain in
 278 Fig. 1, using an amount of averaging corresponding to $L = 58$
 279 independent looks and a coherence threshold of around 0.2.
 280 Phase unwrapping errors are then detected by computing the
 281 difference between the output LoS velocity from the simulated
 282 interferogram and the input (known) velocity field. The only
 283 phase contributions in this difference are unwrapping errors
 284 and phase noise. The estimated standard deviation of the
 285 phase noise for a coherence of 0.2 and $L = 58$ equivalent
 286 number of looks (corresponding to the applied multi-looking)
 287 is $\sigma_n(L) = 0.52$ rad. The coherence of 0.2 leads to an
 288 upper-bound noise estimate, as lower coherence pixels are
 289 masked out in the unwrapping process. To account for phase
 290 noise, unwrapping errors are classified as pixels for which the
 291 difference between the resulting unwrapped phase, ϕ_{unw} , and
 292 the known motion contribution, ϕ_{def} , satisfies:

$$|\phi_{unw} - \phi_{def}| > 2\pi - 3\sigma_n(L) = 4.71 \text{ rad} \quad (2)$$

293 Note that the unwrapping errors detected in the simulation
 294 arising from the coherence estimate for a given image pair are
 295 not necessarily identical to those occurring in the unwrapping
 296 of the interferogram formed from the same imagery. This
 297 is due to the fact that the simulation generates, for each
 298 pixel, a single realization of the complex speckle affecting the

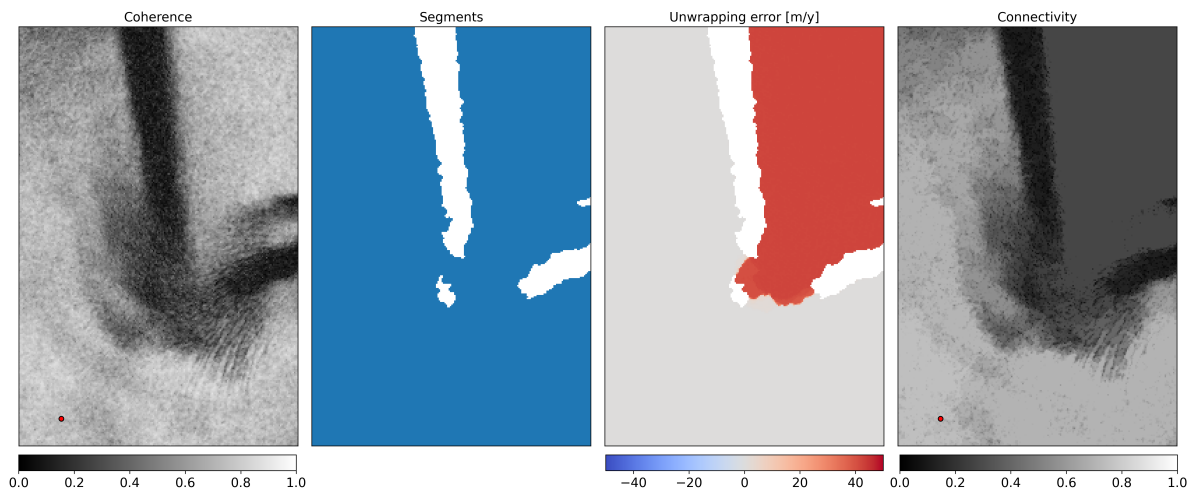


Fig. 2. Example showing (a) coherence, (b) the segment map based on the coherence mask in the unwrapping algorithm, (c) the detected unwrapping error (as described in Section II-A), and (d) the connectivity image derived from the coherence (as described in Section II-B) with the reference point shown by the red dot. The example is a subset from a simulated interferogram (presented in Section III). Note that a large magnitude unwrapping error occurs in a region of high coherence, which is not isolated by the coherence-based mask segmentation, but where connectivity is low.

299 reference and secondary images, based on the real coherence
 300 estimate. Therefore, the simulation results cannot directly be
 301 used to mask errors occurring in the corresponding real in-
 302 terferograms. The simulated interferograms allow for an eval-
 303 uation of the phase unwrapping process, where unwrapping
 304 errors of any magnitude and spatial extent can be detected.

305 Unwrapping errors are more prone to occur further towards
 306 the ice sheet margin, where high shear stresses, caused by fast-
 307 flowing glaciers, and surface melt lead to loss of coherence.
 308 To evaluate the distribution of unwrapping errors and the
 309 performance of the masking method in such a setting, we
 310 selected a slice from an ascending Sentinel-1 track (relative
 311 orbit 74, Interferometric Wide (IW) swath mode, and HH-
 312 polarization) with 13 bursts in each of the three IW swaths,
 313 shown by the purple rectangle in Fig. 7. This slice covers
 314 an area downstream of the Northeast Greenland Ice Stream
 315 (NEGIS), near the outlets of the Zachariae and Nioghalvfjerd-
 316 s-fjorden glaciers. We then carried out the simulation procedure
 317 described in the Appendix for all possible 6-day interfero-
 318 grams using all acquisitions from the year 2017, leading to
 319 a total of 60 simulated interferograms. The TanDEM-X 90
 320 m Greenland DEM [19] and a 2016-2019 average velocity
 321 mosaic based on amplitude tracking measurements generated
 322 through PROMICE (Programme for Monitoring of the Green-
 323 land Ice Sheet) [20] were used in both image coregistration
 324 and interferogram simulations. Figs. 4a and 4b show the
 325 multi-year PROMICE velocity projected to radar LoS and the
 326 average coherence level for the simulated interferograms. The
 327 coherence showed substantial scene-wide variations across
 328 the ensemble of interferograms, meaning that a range of
 329 different conditions are represented (see also Fig. S1 in the
 330 Supplementary Material). For each simulated interferogram,
 331 unwrapping errors were detected by comparing the obtained
 332 LoS velocity measurements with the input external velocity
 333 field, as described above. Figs. 4c and 4d show the frequency
 334 of unwrapping errors and the median error magnitude for

the 60-image pair ensemble observed when not applying the
 the connectivity-based masking method. The Figures illustrate
 how unwrapping errors tend to occur in areas that are confined
 by low coherence regions, generally caused by shear margins.
 Errors are thus observed within the downstream part of the ice
 stream and in the slow-moving region east of the stream. In the
 latter, unwrapping errors are more frequent, however they also
 show a lower median magnitude, compared to the errors within
 the ice stream. Note that as part of the unwrapping algorithm,
 some pixels are masked out based on coherence level and
 the detection of layover/shadow, as described in Section II-A,
 leading to some areas being masked out in all interferograms.

For each of the simulated interferograms, a connectivity
 map was computed. The same connectivity reference point was
 selected for all interferograms (indicated by the red point in
 Fig. 4), in a region towards the interior ice sheet, where veloc-
 ity is low, coherence is typically high, and unwrapping errors
 are not expected to occur. A range of connectivity thresholds
 were then used to generate a mask for each interferogram.
 Based on results from a selection of test image pairs, the
 structuring element for morphological closing of the masks
 was selected as a 32×32 pixel diamond. As unwrapping
 errors can be detected at a pixel level, the performance of the
 connectivity masks can be quantitatively evaluated (Fig. S2 in
 the Supplementary Material shows examples of connectivity
 estimates and masking results for individual image pairs).
 To determine the best performing connectivity threshold, we
 compute the recall and precision measures obtained with
 connectivity thresholds in the range $[0.20; 0.50]$, measured in
 increments of 0.05. Recall is defined as the number of true
 errors detected divided by all true errors in the ensemble,
 while precision is defined as the number of true errors detected
 divided by all detected errors. Hence, in this context, recall can
 be considered the estimated probability that a pixel affected
 by an unwrapping error actually gets masked out, whereas
 precision is the estimated probability that a pixel drawn from

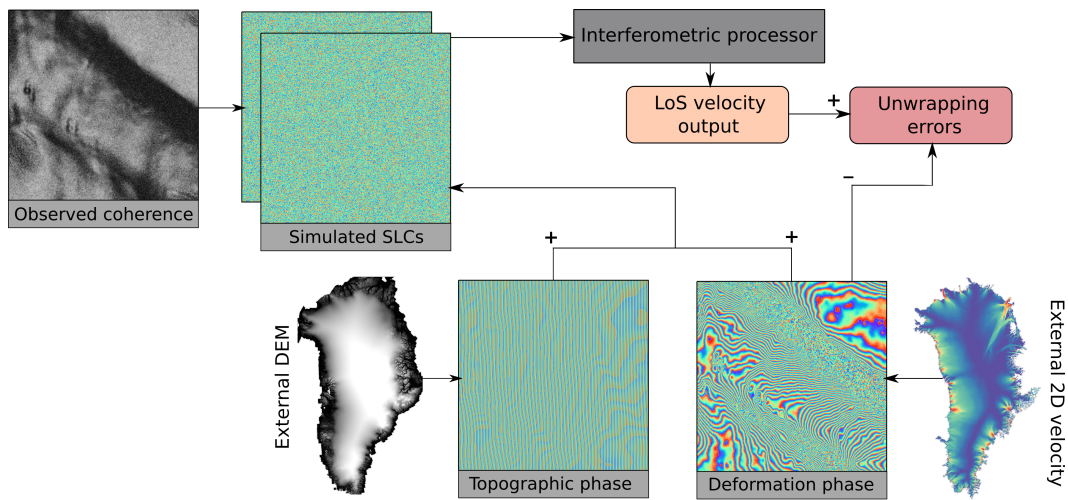


Fig. 3. Flow chart illustrating the process of interferogram simulation, which is further described in the Appendix. The two Single Look Complex (SLC) images are simulated based on a coherence estimate from a real image pair, and a known velocity field is added to the differential phase, such that unwrapping errors can be detected through the difference between the input and output LoS velocity.

371 all the masked pixels is affected by an unwrapping error. The
 372 goal of the masking algorithm is to maximize both of these
 373 measures. A high recall indicates that the masking algorithm is
 374 effective at detecting unwrapping errors, while a high precision
 375 means that few valid pixels are masked. Naturally, recall will
 376 increase with increasing connectivity thresholds, approaching
 377 1 in the trivial case where all pixels are masked out, leading
 378 to 100% of errors being detected. Conversely, for very high
 379 connectivity thresholds, precision will decrease, since more
 380 and more valid pixels will be labelled as errors. To determine
 381 the connectivity threshold which achieves the best balance
 382 between recall and precision the F_β -score can be applied. It
 383 is defined as

$$F_\beta = (1 + \beta^2) \frac{\text{precision} \cdot \text{recall}}{\beta^2 \cdot \text{precision} + \text{recall}} \quad (3)$$

384 and is a measure of effectiveness of the masking assuming
 385 β times as much importance is attached to recall as precision.
 386 In this case, we argue that a selection of $\beta > 1$ is sensible,
 387 meaning that a higher emphasis is put on minimizing the
 388 number of missed unwrapping errors (high recall), rather than
 389 minimizing the number of false detections (high precision).
 390 Here, we opt to use the F_2 -score ($\beta = 2$) as a quality
 391 measure to be maximized. Table I shows the estimated recall,
 392 precision, and F_2 -score, computed for all pixels in the 60-
 393 image pair ensemble and various connectivity thresholds. The
 394 Table shows that recall increases substantially until $\epsilon_c = 0.30$,
 395 after which smaller improvements are observed. Precision is
 396 maximized at a threshold of 0.25-0.30 and then steadily drops,
 397 reflecting the increase in false detections for higher thresholds.
 398 The F_2 -score reaches a maximum at $\epsilon_c = 0.30$, which is thus
 399 deemed the best performing connectivity threshold. For higher
 400 thresholds, the minor improvement in recall is canceled out by
 401 the decrease in precision, leading to an overall decrease in F_2 -
 402 score. Note that the precision of 0.52 means that almost half
 403 of the discarded measurements actually do not contain errors.
 404 While arguably a high price to pay to detect the majority of

TABLE I
 STATISTICS ILLUSTRATING THE PERFORMANCE OF CONNECTIVITY
 MASKING WITH DIFFERENT THRESHOLDS. THE STATISTICS ARE BASED ON
 ALL PIXELS FROM THE 60 SIMULATED INTERFEROGRAMS.

Threshold	Recall	Precision	F2-score	Median error mag.
No masking	-	-	-	40.5 m/y
0.20	0.17	0.46	0.19	27.0 m/y
0.25	0.62	0.53	0.55	3.4 m/y
0.30	0.84	0.52	0.75	1.7 m/y
0.35	0.92	0.42	0.74	1.7 m/y
0.40	0.93	0.35	0.70	1.7 m/y
0.45	0.97	0.29	0.67	1.7 m/y
0.50	0.99	0.25	0.62	3.4 m/y

unwrapping errors, a mitigating circumstance is that tracking
 based methods may provide coverage were DInSAR mea-
 surements are discarded (although with a substantially lower
 accuracy). Recall and precision do not consider the magnitude
 of the unwrapping errors. As seen in Table I, the median
 magnitude of remaining errors shows a substantial drop as
 the threshold is increased, suggesting that larger unwrapping
 errors are associated with lower connectivity levels.

Fig. 5 shows the distribution of connectivity, distinguishing
 between unwrapping errors and valid pixels, and median
 unwrapping error magnitude versus connectivity value for all
 pixels in the simulated interferogram ensemble. The vast ma-
 jority of unwrapping errors are associated with a connectivity
 below 0.30, although a substantial amount of pixels below
 this threshold do not contain errors, as also indicated by
 the precision and recall values in Table I. Additionally, the
 median magnitude of unwrapping errors associated with a
 connectivity above 0.30 is 1.7 m/y (in fact, more than 90%
 of these unwrapping errors have a magnitude of either 1 or
 2 phase cycles, corresponding to 1.7 m/y and 3.4 m/y, re-
 spectively). Conversely, the median magnitude of unwrapping
 errors below 0.30 connectivity is 47.2 m/y. Finally, Fig. 6

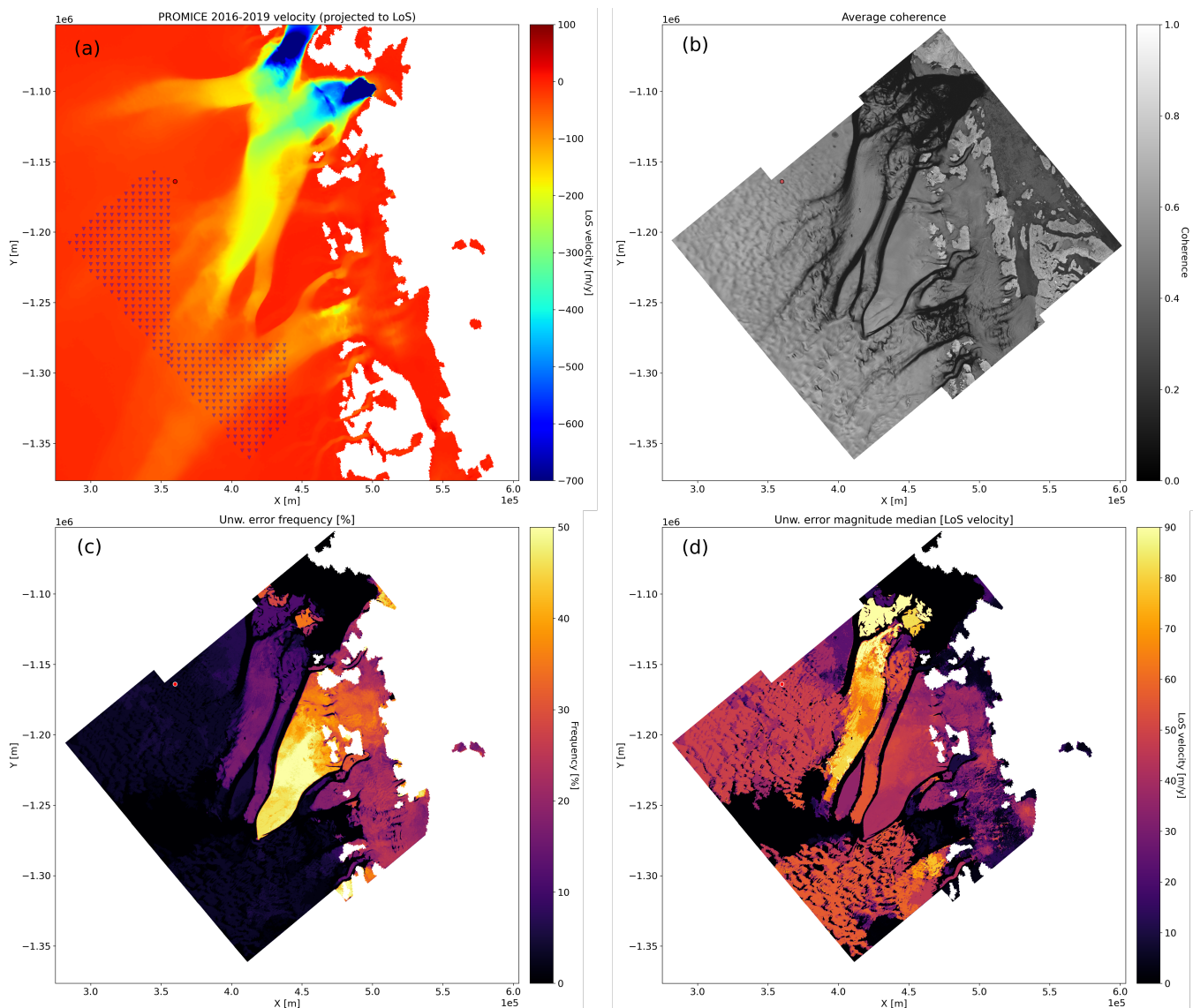


Fig. 4. (a) PROMICE 2016-2019 average velocity [20] projected to the scene line-of-sight, (b) average coherence, (c) unwrapping error frequency, and (d) median unwrapping error magnitude for the simulated interferogram ensemble (60 image pairs in total) without applying connectivity-based masking. Transparent pixels indicate areas where data was discarded in all interferograms due to low coherence or areas where the PROMICE mosaic does not contain measurements (including pixels over ocean). The red dot indicates the connectivity reference point, used for all simulated interferograms, and blue triangles in (a) indicate GCPs used for 0th order calibration of the output velocity measurements.

427 shows the observed unwrapping error frequency and average
 428 magnitude obtained by applying connectivity masking with
 429 thresholds 0.25, 0.30, and 0.35. Comparing the results with
 430 Fig. 4 demonstrates a substantial reduction in unwrapping
 431 error frequency scene-wide in all three cases. Increasing the
 432 threshold from 0.25 to 0.30 provides a noticeable improvement
 433 in terms of error frequency, whereas further increasing the
 434 threshold to 0.35 leads to an increased masking frequency but
 435 only a relatively small reduction in error frequency, as also
 436 indicated by the observed values in Table I.

437 IV. APPLICATION EXAMPLE: NORTHEAST GREENLAND 438 ICE STREAM

439 The connectivity masking approach was also applied to real
 440 image pairs. To this end, we acquired Sentinel-1 IW data

441 in HH-polarization from two ascending and three descending
 442 tracks over the downstream portion of NEGIS spanning the
 443 period 1st December 2019 to 27th January 2020 (see Fig. 7 and
 444 Table II), allowing for the retrieval of the average horizontal
 445 velocity field with application of the surface-parallel flow
 446 assumption [21]. For each of the image pairs, interferometric
 447 processing was carried out as outlined in Section II-A with
 448 multi-looking corresponding to $L = 58$ independent looks.
 449 Connectivity was then estimated, with the reference point for
 450 each track indicated in Fig. 7, and the same threshold was
 451 applied in the masking of all image pairs. The reference points
 452 were selected based on the same rationale as in Section III,
 453 namely that they are in regions towards the interior parts of
 454 the ice sheet where coherence tends to be high and velocity is
 455 low. Based on the results from the simulated data (Section

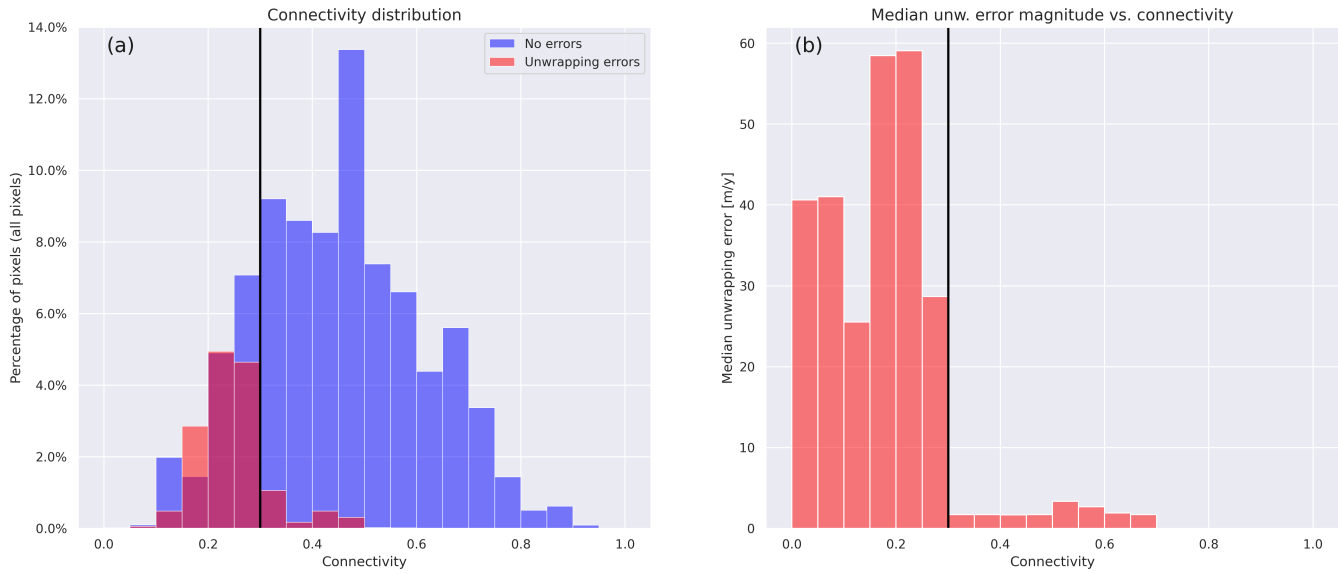


Fig. 5. (a) Histogram showing the distribution of connectivity values (distinguishing between pixels with and without detected unwrapping errors) for all pixels in the simulated interferogram ensemble and (b) bar plot showing median unwrapping error magnitude sorted by connectivity value (in bins with a width of 0.05) for all unwrapping error pixels in the simulated interferogram ensemble. In both plots, the black line indicates connectivity equal to 0.30. Note that bars in (a) are semi-transparent, such that magenta indicates overlapping bars.

TABLE II
OVERVIEW OF SENTINEL-1 DATA PRESENTED IN SECTION IV. ALL IMAGES ARE IN IW MODE AND HH-POLARIZATION. THE SPATIAL EXTENT OF EACH TRACK IS SHOWN IN FIG. 7.

Track	Cycles	Acquisition dates
74 (asc.)	A: 187-191, B: 116-121	1 Dec. 2019 - 24 Jan. 2020
83 (desc.)	A: 188-191, B: 118-120	20 Dec. 2019 - 25 Jan. 2020
89 (asc.)	A: 188-191, B: 116-120	2 Dec. 2019 - 25 Jan. 2020
112 (desc.)	A: 187-191, B: 116-121	4 Dec. 2019 - 27 Jan. 2020
170 (desc.)	A: 186-191, B: 116-120	8 Dec. 2019 - 27 Jan. 2020

III), we chose to test the following subset of connectivity thresholds, $\epsilon_c = \{0.25, 0.30, 0.35\}$. A diamond-shaped structuring element of 32×32 pixels was once again used in the morphological closing of each mask.

Fig. 8 shows the magnitude of the horizontal velocity field inferred from all processed tracks (following the same inversion approach outlined in [5]), both with and without connectivity masking. Also shown is the difference between the velocity magnitude from the obtained measurements and the multi-year average PROMICE map, based on amplitude offset tracking. Differences between these velocity fields may be caused by unwrapping errors, temporal variations in the velocity field, atmospheric effects, and calibration errors. Inspecting 8b, reveals several contiguous areas of high magnitude differences, most of which are in regions that, based on the simulation experiments, are expected to be prone to unwrapping errors. The sharp gradients surrounding these areas suggest that they are likely caused by unwrapping errors, rather than e.g. seasonal velocity variations or calibration errors. Figs. 8d and 8f show how some of the suspected unwrapping errors are eliminated with a connectivity threshold

of 0.25, while setting $\epsilon_c = 0.30$ appears to eliminate all the major (suspected) unwrapping errors. Note that some measurements, which based on the velocity difference measure are not expected to be unwrapping errors, are also discarded by the connectivity masking in both cases (for instance in the upstream part of NEGIS). This is also in line with expectations based on the simulation experiments, where a precision on the order of 0.5 was estimated for the presented connectivity thresholds. Although coherence is generally expected to be higher in winter months, many of the 6-day interferograms in this data set show moderately low coherence levels towards the interior ice sheet (see Fig. S3 in the Supplementary Material). While these coherence levels seemingly do not lead to unwrapping errors, they do lead to low connectivity levels and consequently to the discarding of valid measurements and a lowered precision. The case of $\epsilon_c = 0.35$ is not shown, as the 0.30 threshold already seems to detect the vast majority of errors.

V. DISCUSSION

An advantage of the connectivity masking approach is that it allows for an automated masking of each individual interferogram, independent of external data sets. Hence, instead of discarding all measurements from a region that is expected to be prone to unwrapping errors (as would be common practice), one can apply connectivity masking and achieve DInSAR velocity measurements with high reliability. We tested the method in the downstream part of NEGIS, an area where features often associated with unwrapping errors (such as high levels of shear, ice-bedrock transitions, and frequent loss of coherence) are well represented. Although the ensemble of simulated interferograms all cover the same region, a wide variety of coherence (and hence unwrapping error) realizations are observed, allowing evaluation of the connectivity masking

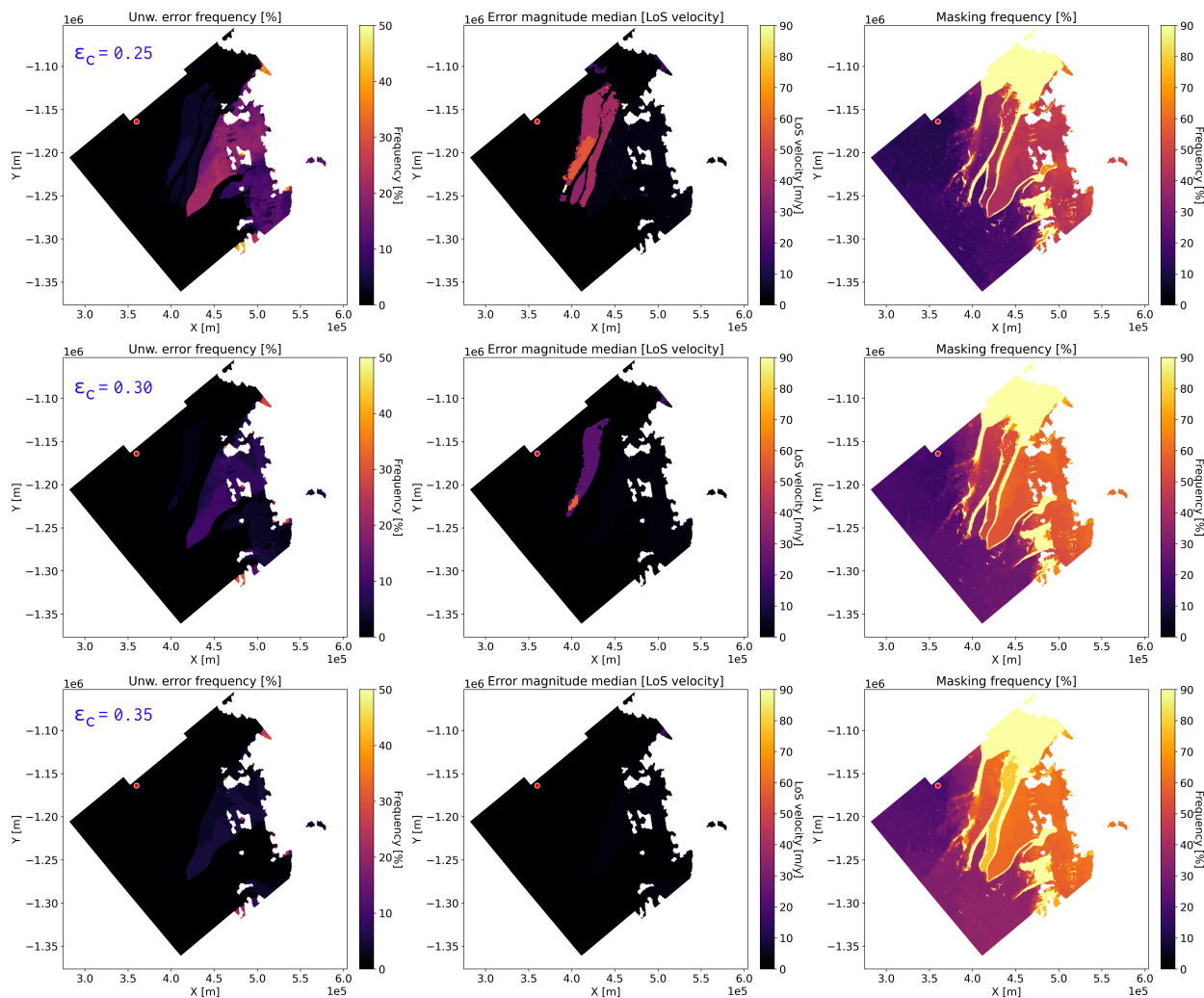


Fig. 6. Unwrapping error frequency (left column), average error (middle column), and masking frequency (right column) for the simulated interferogram ensemble after connectivity masking with a threshold of 0.25 (top row), 0.30 (middle row), and 0.35 (bottom row).

510 approach under different conditions. It is possible that the
 511 masking performance and the optimal connectivity threshold
 512 might show some variation for a different distribution of
 513 coherence realizations or for different geographical regions.

514 The connectivity measure generally captures unwrapping
 515 errors well, with most error pixels in the simulated data set
 516 being associated with lower connectivity values. As indicated
 517 by Table I and Fig. 5b, when applying a 0.30 connectivity
 518 threshold, a majority of missed detections have an error mag-
 519 nitude of a single phase cycle (1.7 m/y). Fig. S2 in the Sup-
 520 plementary Material shows the connectivity and unwrapping
 521 error occurrences for some of the simulated interferograms.
 522 For one of these interferograms, an error of a single phase
 523 cycle occurs in a large region where connectivity is moderately
 524 high, meaning that it remains undetected by the connectivity
 525 masking. Based on our observations, the connectivity masking
 526 approach is generally more effective at detecting unwrapping
 527 errors of large spatial scales and large magnitudes. The mor-
 528 phological closing, which is applied to reduce the number of
 529 valid measurements discarded, may lead to missed detections
 530 of unwrapping errors at a scale smaller than the structuring

element.

531
 532 As mentioned in Section II-B, several coherence weight-
 533 ing functions were tested in the generation of a confidence
 534 measure for the connectivity estimation, although we found
 535 unweighted coherence to perform the best. It is, of course,
 536 also possible to combine different parameters or external data
 537 sets in the confidence measure, as long as the final measure
 538 is normalized to an interval of [0;1], however this was not
 539 thoroughly investigated in this study.

540 In the evaluation of the best performing connectivity thresh-
 541 olds, we weighted recall higher than precision, arguing that
 542 missing the detection of unwrapping errors comes at a higher
 543 price than discarding valid measurements. Consequently, the
 544 threshold of 0.30, which we deemed optimal for both simu-
 545 lated and real data, has an estimated precision of 0.52, mean-
 546 ing that nearly half of the discarded measurements are valid. Since
 547 amplitude tracking either way must be carried out to cover
 548 fast-flowing parts of glaciers, these measurements can be used
 549 to provide coverage in regions where DInSAR measurements
 550 are discarded, albeit at a lower resolution and accuracy.
 551 However, if DInSAR and tracking-based measurements are

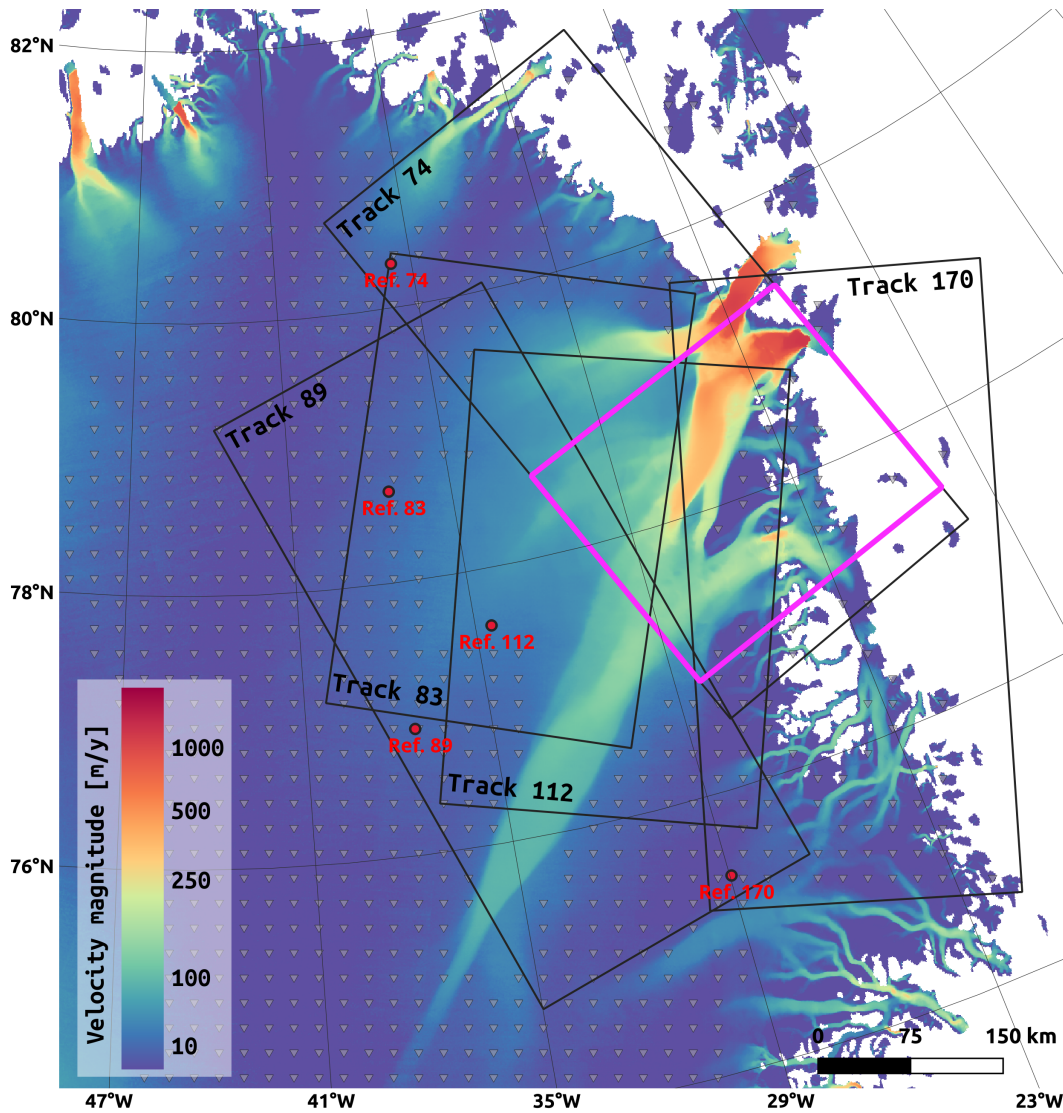


Fig. 7. Overview of the Sentinel-1 data processed in this study (shown in map projection EPSG:3413). Black rectangles indicate Sentinel-1 tracks used to estimate 2D velocity over part of the Northeast Greenland Ice Stream (presented in Section IV), whereas the magenta rectangle indicates the subset processed for the simulated interferograms (presented in Section III). Ground Control Points used for calibration are shown as gray triangles and red points indicate connectivity reference points. The color scale indicates velocity magnitude from the Programme for Monitoring of the Greenland Ice Sheet (PROMICE) 2016-2019 average mosaic.

552 combined using weights that are inversely proportional to
 553 the estimated accuracy, as in e.g. [5], DInSAR measurements
 554 will dominate the resulting velocity field wherever they are
 555 available. Hence, measurements containing unwrapping errors
 556 will not be averaged out by the combination with amplitude
 557 tracking measurements but will propagate to the final product,
 558 highlighting the importance of detecting as many unwrapping
 559 errors as possible, especially those of high magnitudes, even at
 560 the cost of low precision. Fortunately, the simulations suggest
 561 that, generally, unwrapping errors of higher magnitudes are
 562 associated with lower connectivity levels (Table I and Fig. 5),
 563 increasing the likelihood of detecting larger errors.

564 In the cases presented here, the reference point for con-
 565 nectivity estimation was selected manually as a point to-
 566 wards the interior part of the ice sheet, where coherence
 567 is typically higher and unwrapping errors are not generally

568 expected. The reference point selection could be automated by
 569 selecting the point of maximum coherence within the largest
 570 interferogram segment (following the segmentation process
 571 mentioned in Section II-A). Figs. S4-S5 in the Supplementary
 572 Material show the connectivity maps and unwrapping error
 573 distributions obtained for two of the simulated image pairs
 574 using different reference points, including the reference
 575 point defined by the automated approach. Nearly identical
 576 masking results are obtained for the various reference points,
 577 suggesting a limited sensitivity to the reference point selection.
 578 For very large scenes (e.g. Sentinel-1 tracks extending across
 579 the Greenland Ice Sheet), reference point selection may in
 580 some cases be somewhat complicated, e.g. in case a large
 581 region of low coherence forms a divide between two coherent
 582 regions. In such a case, it may be beneficial to divide the scene
 583 in smaller subsets and process these separately. Automation

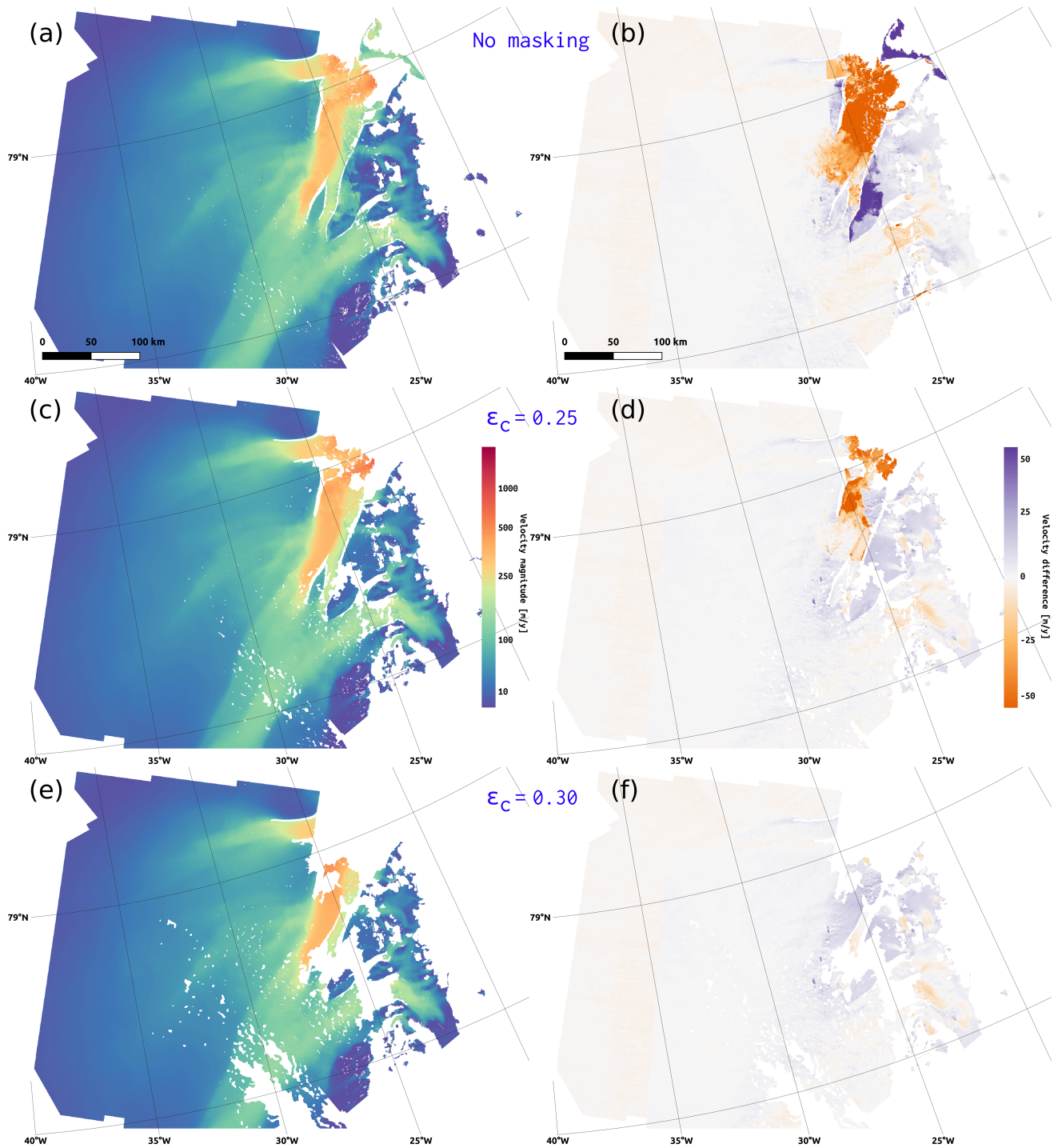


Fig. 8. Horizontal velocity magnitude for the period 1st December 2019 to 27th January 2020 obtained from the NEGIS Sentinel-1 image pairs shown in Table II and Fig. 7 (left column) and difference in horizontal velocity magnitude with respect to the PROMICE multi-year mosaic (right column) in the case of no masking (top row) and connectivity masking with a threshold of 0.25 (middle row) and 0.30 (bottom row). In both masking cases, a morphological closing with a 32×32 pixel diamond-shaped structuring element was applied.

584 of such a process should be further investigated before the
 585 connectivity-masking approach is applied in a fully ice sheet-
 586 wide operational manner.

587 VI. CONCLUSION

588 The occurrence of unwrapping errors is one of the most
 589 significant sources of error in DInSAR ice velocity retrieval,

specifically affecting measurements towards the ice sheet margin,
 near glacier outlets. As demonstrated here, conventional
 methods such as coherence-based masking and segmentation
 alone are not sufficient to fully prevent unwrapping errors. We
 propose a masking approach based on pixel connectivity estimation,
 adapted from the work of [13], to improve detection of unreliable
 DInSAR measurements. In this approach, a mask

is generated for each individual interferogram by masking out pixels with a connectivity below a certain threshold, specified by the user. The connectivity estimate is based solely on the interferometric coherence and a single reference point and hence does not require a full DInSAR time series to be processed, nor does it rely on external data sets. For the examples presented here, the connectivity reference point selection was done manually, however we argue that this process can be automated by selecting the point of maximum coherence in the largest interferogram segment. Results obtained for both simulated and real data suggest that a reasonable connectivity threshold is on the order of 0.30. With such a threshold, we estimate a recall of 0.84 and a precision of 0.52, indicating that the vast majority of unwrapping errors are detected, although nearly half of the discarded measurements are not actually affected by unwrapping errors. In ice sheet-wide routine retrievals, DInSAR measurements are, ideally, combined with tracking-based measurements. As the coverage of the tracking-based methods is better than that obtained by DInSAR, coverage may still be achieved in areas that are flagged by the connectivity-based masking. Therefore, we prioritize masking the majority of unwrapping errors even at the cost of discarding some valid DInSAR measurements. Finally, we observe a tendency for unwrapping errors of higher magnitudes to be associated with pixels of lower connectivity values, with the simulated interferogram ensemble showing a median error of only 1.7 m/y for pixels with connectivity above 0.30. Hence, larger unwrapping errors are more likely to be detected, even when masking with relatively low connectivity thresholds.

APPENDIX INTERFEROGRAM SIMULATION

For each interferogram, the simulation procedure is as follows: 1) Carry out a refined coregistration of a real Sentinel-1 data pair, as described in [5], [6]. 2) Estimate interferometric coherence, applying multi-looking with a factor of 18×4 in range \times azimuth. The coherence estimate is then interpolated (using inverse distance weighting) to full resolution in the geometry of the first SLC. 3) Simulate two complex SLCs, u_1 and u_2 , in the same geometry and with the same coherence as the real data pair, according to [22]:

$$u_1 = \sqrt{1-\gamma}a + \sqrt{\gamma}c \quad (4)$$

$$u_2 = \sqrt{1-\gamma}b + \sqrt{\gamma}c \quad (5)$$

where a , b , and c are uncorrelated stationary white complex Gaussian processes of equal (unit) variance and γ is the estimated coherence. 4) Add deterministic phase contributions representing the flat-earth term, the topography, and the deformation to the first SLC image:

$$u_1^{det} = u_1 e^{j(\phi_{flat} + \phi_{topo} + \phi_{def})} \quad (6)$$

The flat-earth and topographic contributions, ϕ_{flat} and ϕ_{topo} , are estimated through precise orbits and an external DEM, whereas the deformation phase term is computed as:

$$\phi_{def} = -\frac{4\pi}{\lambda} v_{LoS} \Delta T \quad (7)$$

where λ is the radar wavelength, v_{LoS} is the line-of-sight velocity component, and ΔT is the temporal baseline, which is equal to 6 days for all the interferograms presented here. The line-of-sight velocity is computed by projecting an external ice velocity mosaic, e.g. a multi-year velocity average, on the radar line-of-sight. Atmospheric phase contributions are neglected, as these generally do not lead to unwrapping errors. 5) Finally, the simulated SLCs enter a usual DInSAR processing scheme (omitting coregistration, as this has already been done prior to the coherence estimation). The interferogram is formed as:

$$I^{sim} = u_1^{det} u_2^* \quad (8)$$

and once flattening is carried out, based on the same orbit files and DEM applied in the simulations, the only remaining phase contributions are the deformation term, which is known, and the phase noise corresponding to the coherence estimate.

ACKNOWLEDGMENT

The PROMICE multi-year average ice velocity mosaic was generated by Anne M. Solgaard, GEUS. Sentinel-1 data is provided by the EU Copernicus Programme. Interferometric processing was carried out using the DTU Space inhouse processing software (IPP).

REFERENCES

- [1] I. Joughin, B. E. Smith, and I. M. Howat, "A complete map of Greenland ice velocity derived from satellite data collected over 20 years," *Journal of Glaciology*, vol. 64, no. 243, pp. 1–11, 2018.
- [2] J. Mouginit, E. Rignot, and B. Scheuchl, "Continent-wide, interferometric SAR phase, mapping of Antarctic ice velocity," *Geophysical Research Letters*, vol. 46, pp. 9710–9718, 2019.
- [3] T. Nagler, H. Rott, M. Hetzenecker, J. Wuite, and P. Potin, "The Sentinel-1 mission: New opportunities for ice sheet observations," *Remote Sensing*, vol. 7, pp. 9371–9389, 2015.
- [4] F. De Zan, P. Prats-Iraola, R. Scheiber, and A. Rucci, "Interferometry with TOPS: Coregistration and Azimuth Shifts," in *Proceedings of EUSAR 2014*, 2014, pp. 949–952.
- [5] J. Andersen, A. Kusk, J. Boncori, C. Hvidberg, and A. Grinsted, "Improved ice velocity measurements with Sentinel-1 TOPS interferometry," *Remote Sensing*, vol. 12, no. 12, 2020.
- [6] A. Kusk, J. K. Andersen, and J. P. M. Boncori, "Burst overlap coregistration for Sentinel-1 TOPS DInSAR ice velocity measurements," *IEEE Geoscience and Remote Sensing Letters*, 2021.
- [7] C. Werner, U. Wegmüller, and T. Strozzi, "Processing Strategies for Phase Unwrapping for InSAR Applications," in *Proceedings of EUSAR 2002*, 2002, pp. 353–355.
- [8] M. Eineder, "Efficient Simulation of SAR Interferograms of Large Areas and of Rugged Terrain," *IEEE Transactions on Geoscience and Remote Sensing*, vol. 41, no. 6, pp. 1415–1427, 2003.
- [9] E. Weber Hoen and H. Zebker, "Penetration depths inferred from interferometric volume decorrelation observed over the greenland ice sheet," *IEEE Transactions on Geoscience and Remote Sensing*, vol. 38, no. 6, pp. 2571–2583, 2000.
- [10] O. Hellwich, "SAR Phase Unwrapping: Implications of Terrain Shape and Smoothing," in *Proceedings of EUSAR 1998*, 1998, pp. 51–56.
- [11] R. Goldstein, H. Engelhardt, B. Kamb, and R. Frolich, "Satellite radar interferometry for monitoring ice sheet motion: Application to an antarctic ice stream," *Science*, vol. 262, no. 5139, pp. 1525–1530, 1993.
- [12] H. A. Zebker and J. Villasenor, "Decorrelation in interferometric radar echoes," *IEEE Transactions on Geoscience and Remote Sensing*, vol. 30, no. 5, pp. 950–959, 1992.
- [13] L. Galli, "A new approach based on network theory to locate phase unwrapping unreliable results," in *Proceedings of IGARSS 2001*. IEEE, 2001, Proceedings Paper, pp. 118–120.

- 706 [14] A. Kusk, J. Boncori, and J. Dall, "An automated system for ice
707 velocity measurement from SAR," in *Proceedings of EUSAR 2018*, ser.
708 *Proceedings of the European Conference on Synthetic Aperture Radar*.
709 VDE Verlag, 2018, pp. 929–932.
- 710 [15] J. J. Mohr and J. P. M. Boncori, "An error prediction framework
711 for interferometric SAR data," *IEEE Transactions on Geoscience and*
712 *Remote Sensing*, vol. 46, no. 6, pp. 1600–1613, 2008.
- 713 [16] M. Costantini, "A novel phase unwrapping method based on network
714 programming," *IEEE Transactions on Geoscience and Remote Sensing*,
715 vol. 36, no. 3, pp. 813–821, 1998.
- 716 [17] M. Hubig, S. Suchandt, and M. Eineder, "Automatic correction of
717 baseline and phase unwrapping errors in SAR interferograms," in
718 *Proceedings of EUSAR 2000*, 2000, pp. 131–134.
- 719 [18] E. W. Dijkstra, "A note on two problems in connexion with graphs,"
720 *Numerische Mathematik*, vol. 1, no. 1, pp. 269–271, 1959.
- 721 [19] P. Rizzoli, M. Martone, C. Gonzalez, C. Wecklich, D. B. Tridon,
722 B. Bräutigam, M. Bachmann, D. Schulze, T. Fritz, M. Huber, B. Wessel,
723 G. Krieger, M. Zink, and A. Moreira, "Generation and performance
724 assessment of the global TanDEM-X digital elevation model," *ISPRS*
725 *Journal of Photogrammetry and Remote Sensing*, vol. 132, pp. 119–
726 139, 2017.
- 727 [20] A. Solgaard, A. Kusk, J. P. M. Boncori, J. Dall, K. D. Mankoff, A. P.
728 Ahlstrøm, S. B. Andersen, M. Citterio, N. B. Karlsson, K. K. Kjeldsen,
729 N. J. Korsgaard, S. H. Larsen, and R. S. Fausto, "Greenland ice velocity
730 maps from the PROMICE project," *Earth System Science Data*, vol. 13,
731 no. 7, pp. 3491–3512, 2021.
- 732 [21] I. Joughin, R. Kwok, and M. Fahnestock, "Interferometric estimation
733 of three-dimensional ice-flow using ascending and descending passes,"
734 *IEEE Transactions on Geoscience and Remote Sensing*, vol. 36, no. 1,
735 pp. 25–37, 1998.
- 736 [22] R. Bamler, "Interferometric stereo radargrammetry: absolute height
737 determination from ERS-ENVISAT interferograms," in *Proceedings of*
738 *IGARSS 2000*, vol. 2, 2000, pp. 742–745.



765 **Anders Kusk** received the M.Sc. degree in electrical
766 engineering at the Technical University of Denmark,
767 in 2002. In 2006, he received the Ph.D. degree,
768 working on SAR processing techniques at the Tech-
769 nical University of Denmark, where he continued to
770 work as a postdoctoral researcher. Since 2009, he
771 has worked at the Microwaves and Remote Sensing
772 division of DTU Space, Technical University of
773 Denmark, as a research engineer. His research inter-
774 ests include ice flow mapping from SAR data within
775 the ESA Icesheets CCI (Climate Change Initiative)
776 project and the national Danish PROMICE project (Programme for Monitoring
777 of the Greenland Ice Sheet). He also participates in system development,
778 processor development, and campaign activities for ESA's P-band Polarimetric
779 Airborne Radar Ice Sounder, POLARIS.

739
740
741
742
743
744
745
746
747
748
749



750 **Jonas Kvist Andersen** received the M.Sc. Eng.
751 degree in Earth and Space Physics and Engineering
752 at the Technical University of Denmark, in 2019.
753 Since 2019 he has been pursuing the Ph.D. degree
754 at the Microwaves and Remote Sensing division
755 of DTU Space, Technical University of Denmark,
756 working on applying SAR interferometric techniques
757 for Sentinel-1 TOPS-mode ice velocity retrieval. He
758 has contributed to research collaborations with e.g.
759 the European Space Agency and the Geological
760 Survey of Denmark and Greenland.

750
751
752
753
754
755
756
757
758
759
760
761
762
763
764



750 **John Peter Merryman Boncori** received the "Lau-
751 rea" degree in communications engineering (summa
752 cum laude) from the University of Rome "Tor Ver-
753 gata," Rome, Italy, in 2003, and the Geoinformation
754 Ph.D. degree from the University of Rome "Tor
755 Vergata," in 2007. Since then he has worked as
756 a researcher at both the Technical University of
757 Denmark and the National Institute of Geophysics
758 and Volcanology in Italy. Since 2017 he has been an
759 associate professor at the Microwaves and Remote
760 Sensing division of DTU Space, Technical Univer-
761 sity of Denmark, where he has also served as head of division since 2020. He
762 has worked on a range of international research projects related to SAR data
763 processing as well as interferometric SAR techniques and their application in
764 measurements of e.g. seismic deformation and ice flow.